EVALUATION OF REGIONAL TRAVEL-TIME AND LOCATION IMPROVEMENT ALONG THE TETHYAN MARGIN USING A NEW THREE-DIMENSIONAL VELOCITY MODEL

Sung-Joon Chang [1], Megan P. Flanagan[2], Suzan van der Lee[1], Eric M. Matzel[2], and Michael E. Pasyanos[2]

Northwestern University[1] and Lawrence Livermore National Laboratory[2]

Sponsored by National Nuclear Security Administration

Contract Nos. DE-FC52-04NA25541[1] and DE-AC52-07NA27344[2]
Proposal No. BAA04-40

ABSTRACT

For purposes of studying the lateral heterogeneity as well as predicting seismograms for this region, we construct a new 3-D S-velocity model by jointly inverting a variety of different seismic data. We jointly invert regional waveforms, surface wave group velocity measurements, teleseismic *S* and *SKS* arrival times, and crustal thickness estimates from receiver functions, refraction lines, and gravity surveys. These data types have complementary resolving power for crust and mantle structures, vertical and lateral variations, shallow and deep mantle features, local and global structure. Therefore, a joint inversion of these data sets might help unravel the complexity of this tectonically diverse area. These measurements are made from a combination of MIDSEA, PASSCAL, GeoScope, Geofon, GSN, IDA, MedNet, national networks, and local deployments throughout the study region which extends from the western Mediterranean region to the Hindu Kush and encompasses northern Africa, the Arabian peninsula, the Middle East, and part of the Atlantic Ocean for reference. The Moho depth result is broadly consistent with CRUST2.0, except in mid-northern Africa, where the crust from our joint inversion is about 5 km thinner. Fast velocity anomalies are found beneath the West African Craton, the Hellenic trench, the Apennines, the East European Platform, and the Arabian Platform at a 75–150 km depth, whereas low-velocity anomalies are located along the plate boundaries such as the mid-Atlantic ridge, Afar, the Anatolian Plateau, Iran, Afghanistan, western Mediterranean Sea, and the Red Sea. Based on the assumption that *P*-wave velocity anomalies in m/s scale are very close to *S*-wave velocity anomalies in m/s scale in our study area, we convert our *S*-velocity model to a *P*-velocity model with use of teleseismic *P* arrival times. Finally, our model is validated by performing travel-time predictions with a dataset of ground truth events. Our model generally produces better travel-time predictions than the iasp91 model. We expect that better travel-time predictions may be achieved by replacing the poorly resolved crust in our model with CRUST2.0 and refining the *P*-velocity model.

OBJECTIVES

Our primary objective is developing a new 3-D *S*-velocity model for the Middle East and Mediterranean region, including North Africa, southern Europe, and Arabia that

1) is resolved in aseismic regions;
2) is resolved throughout the upper mantle (to 660 km);
3) resolves laterally varying crustal thickness;
4) contains laterally varying vertical velocity gradients;
5) is simultaneously compatible with multiple data sets;
6) utilizes several recent, unique waveform data sets; and
7) includes uncertainties of the model parameters.

These features would increase the model's ability to predict and calibrate regional travel times and waveforms, thereby providing improved event locations, focal mechanisms, and other event discriminants.

Secondly, we aim to convert the 3-D *S*-velocity model to a 3-D *P*-velocity model, using teleseismic *P*-arrival times.

Our third objective is to test both the *P*-and *S*-wave models' ability to predict regional *P* and *S* travel times, deflect wave paths and deform waveforms, and assess their effects first on the studied seismograms (travel times and amplitudes) and subsequently on the 3-D models derived from these data.

This report covers all the above-mentioned objectives.

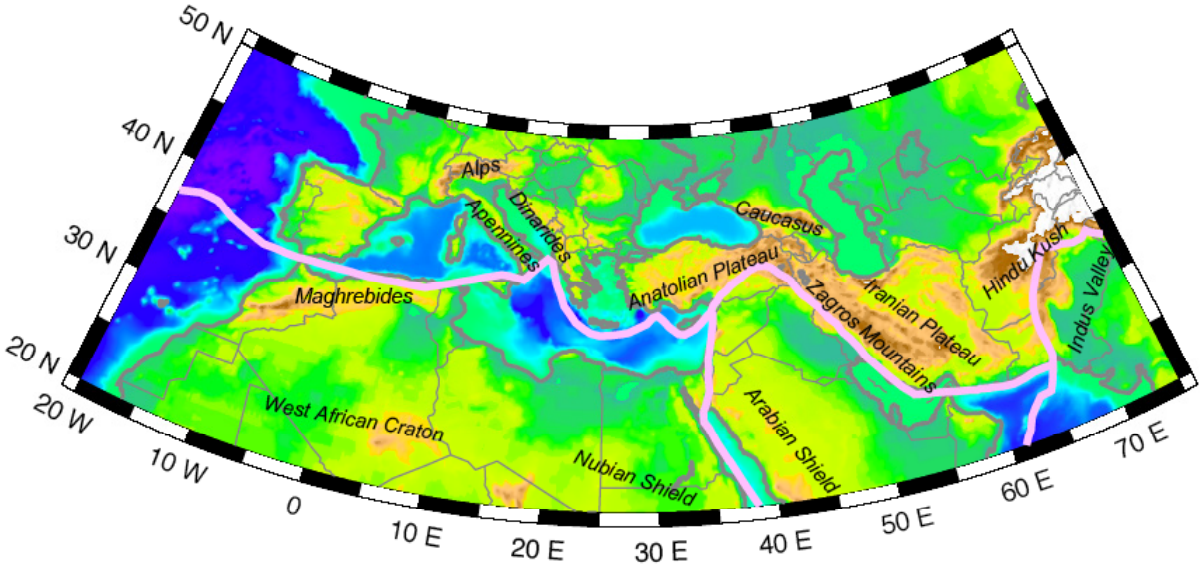

Figure 1. Topographic map of the study region. The pink line is the NUVEL1-A (DeMets et al., 1990) representation of the Eurasia-Africa-Arabia plate boundary.

The study region is centered around the Africa-Arabia-Eurasia triple junction (Figure 1), and extends west to the Africa-Eurasia-North America junction at the Azores, just off the map, and east to the Arabia-Eurasia-Indian Plate junction. The NUVEL1-A (DeMets et al., 1990) representation of these plate boundaries is shown by the pink line in Figure 1. The interaction of these five major tectonic plates with each other and with several microplates within an area of one quarter of the Earth's circumference yields this region rich with tectonic complexity. We plan to capture various renditions of this structurally complicated part of the world in one *S*-velocity model through the joint inversion of several different types of seismic data simultaneously; the new model will refine our understanding of the structure and tectonics in this region of the Earth. The data types we combine are constraints from independent studies on the depth to the Moho, fundamental-mode Rayleigh-wave group velocity measurements, waveform fits of regional *S* and Rayleigh waves, and arrival times of teleseismic *S* and *SKS* waves. We convert the resulting *S*-

velocity model to a *P*-velocity model with over 2.9 million teleseismic *P* arrival times. Then, we validate our model by performing travel-time prediction with a dataset of ground truth event.

RESEARCH ACCOMPLISHED

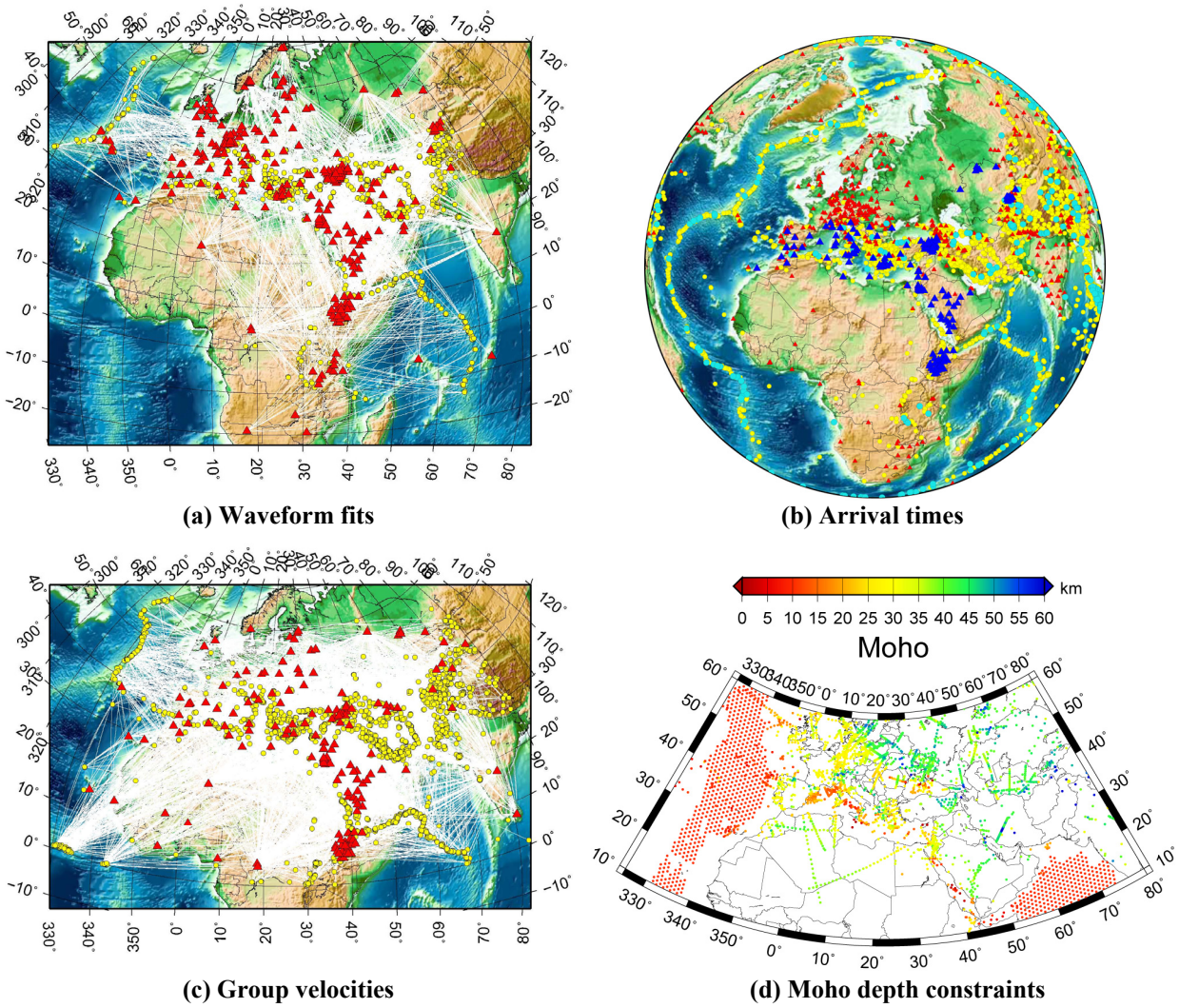

(a) Waveform fits **(b) Arrival times**

(c) Group velocities **(d) Moho depth constraints**

Figure 2. Datasets used for the joint inversion. (a) Ray path coverage for regional waveform fits. Stations are illustrated as red triangles, and events as yellow circles. (b) Events and stations used for teleseismic *S* and *SKS* arrival time estimation. Cyan circles and blue triangles represent events and stations used for relative delay time estimation with MCCC, respectively. Yellow circles and red triangles are events and stations from the reprocessed ISC catalogue. (c) Great-circle wave paths for 45 s period Rayleigh waves. Stations are illustrated as red triangles, and events as yellow circles. (d) Map of the Moho depth distribution acquired from literatures. Artificial point constraints of 10 km depth are placed to the Atlantic and Indian Oceans where measurements are absent.

Regional Waveform Fits

We fit over 5,600 available waveforms from the Lawrence Livermore National Laboratory (LLNL) database and MIDSEA dataset (Marone et al., 2004) which sample the Mediterranean region, North Africa, the Middle East, Pakistan, and Afghanistan using the non-linear inversion procedure employed by partitioned waveform inversion studies (Nolet, 1990; Van der Lee and Nolet, 1997). We utilize events with magnitude larger than 4.0 and seismograms with epicentral distance from 5º to 50º. The great-circle wave paths for these seismograms are shown

in Figure 2(a). We have estimated path-averaged *S*-velocity structures for these paths using the same starting *S*-velocity model but a different crustal thickness (in 5 km increments) for each path, based on a priori reported estimates (Marone et al., 2004). The starting model often predicts significant phase differences relative to the data for both the *S*- and Rayleigh waves. The inversion procedure estimates the perturbations to the starting model by non-linear optimization (Nolet, 1990; van der Lee and Nolet, 1997). For the computation of synthetic waveforms we also need to know the source mechanisms of the events. We typically use the centroid moment tensors (CMT) from the Global CMT project, and hypocenters from Engdahl's reprocessed International Seismological Centre (ISC) database (Engdahl et al., 1998). The frequency content of the data and synthetic is different for each fit and generally falls within the band 0.006 to 0.1 Hz.

Teleseismic *S* and *SKS* Arrival Times

We obtained *S* and *SKS* phase arrival time data from two different sources. Both arrival times are adjusted for topography and Earth's ellipticity before inversion. First, we used high-quality relative arrival times of teleseismic *S* and *SKS* waves (Benoit et al., 2006; Park et al., 2007; Schmid et al., 2004) which are measured on broadband seismograms with use of multi-channel cross-correlation (MCCC; VanDecar and Crosson, 1990). Benoit et al. (2006), Park et al. (2007), and Schmid et al. (2004) used seismograms recorded in the Mediterranean, Ethiopia, amd Saudi Arabia, respectively. Moreover, we measured additional relative delay times at Turkey and central Asia. The number of *S* phase relative arrival times is over 5900 with epicentral distances of 30º–90º and the number of *SKS* phases is over 1,400 with distances of 87º–140º; over 73,00 in total. We set 0.5 s as uncertainty for weights during the inversion. Second, we obtained over 223,000 *S* phase arrival time data from the reprocessed ISC database (Engdahl et al., 1998) from 1964 to 2007. The epicentral distance range is 20º–80º. We set lower uncertainty of 2.5 s for the data because lots of outliers and systematic errors are found in this data set by Röhm et al. (2000). We illustrate location of stations and events for each of the two types of arrival time data in Figure 2(b).

Surface Wave Group Velocities

We have measured over 105,000 group velocities of fundamental-mode Rayleigh waves recorded at MIDSEA and other stations in the region and used them to update previous group velocity maps (e.g., Pasyanos, 2005). Figure 2(c) shows the great-circle wave paths for which we included fundamental-mode Rayleigh wave group velocities in our joint inversion. Compared to other data types we include, lateral coverage is best for this group velocity data set, though vertical coverage is provided mainly by the teleseismic arrival times and regional *S* and Rayleigh waveforms. The period for group velocities ranges from 7 to 100 sec.

Crustal Thickness Constraints

While the fundamental-mode Rayleigh-wave group velocities and regional *S* and Rayleigh waveforms have significant sensitivity to Moho depth, they cannot uniquely resolve Moho depth. We therefore include independent estimates of crustal thickness as point constraints in the joint inversion and thus compile such measurements from a large number of published studies. A partial list of these studies is provided in Marone et al. (2003) and part of these points stem from the database used for CRUST5.1 (Mooney et al., 1998). We have added new estimates of Moho depth from more recent studies and interactively resolved or removed conflicting data and outliers from the data set. Over 4,700 Moho depth constraints are mapped in Figure 2(d). The majority of this data set is from receiver function studies. Remaining points are from active-source studies and some are from gravity surveys. The active-source constraints were assigned relatively low errors and the Moho-depth estimates from gravity were assigned the largest errors. For the oceans we use a constraint of 10 km for Moho depth, but only for points also covered by data from our other data sets.

Inversion Results

We have developed software that handles the joint inversion of constraints from regional waveform fits, crustal estimates, group velocities, and teleseismic arrival times. The resolving power of the combined data is superior to that of each of the data sets alone. The joint inversion reduces the variance in the data sets by 38% for the teleseismic delay times, 55% for the Rayleigh-wave group velocities, 90% for the Moho point constraints, and 88% for the regional waveform fits.

Figure 3 shows the joint inversion results for Moho depth and velocity perturbations. The Moho map shows a good resemblance with the point constraints in Figure 2(d), but is much smoother because the regional waveforms and group velocity data, as well as regularization constraints in the joint inversion provide a smooth interpolation between the point constraints. The map is also broadly consistent with CRUST2.0, except in northern Africa, where the crust from our joint inversion is about 5 km thinner. Resolution tests indicate that our combined data sets can resolve the crustal thicknesses of CRUST2.0.

Fast-velocity anomalies are found beneath the West African Craton, the Hellenic trench, the Apennines, the East European Platform, and the Arabian Platform at 75–150 km depth, whereas low-velocity anomalies are located along the plate boundaries such as the mid-Atlantic ridge, Afar, the Anatolian Plateau, Iran, Afghanistan, western Mediterranean Sea, and the Red Sea. Fast-velocity anomalies are spread beneath the western Mediterranean Sea, Dinarides, the Aegean Sea, Turkey, and the Black Sea at a 500-km depth, which may indicate subducting slabs from the Apennine, the Calarian arc, and the Hellenic arc.

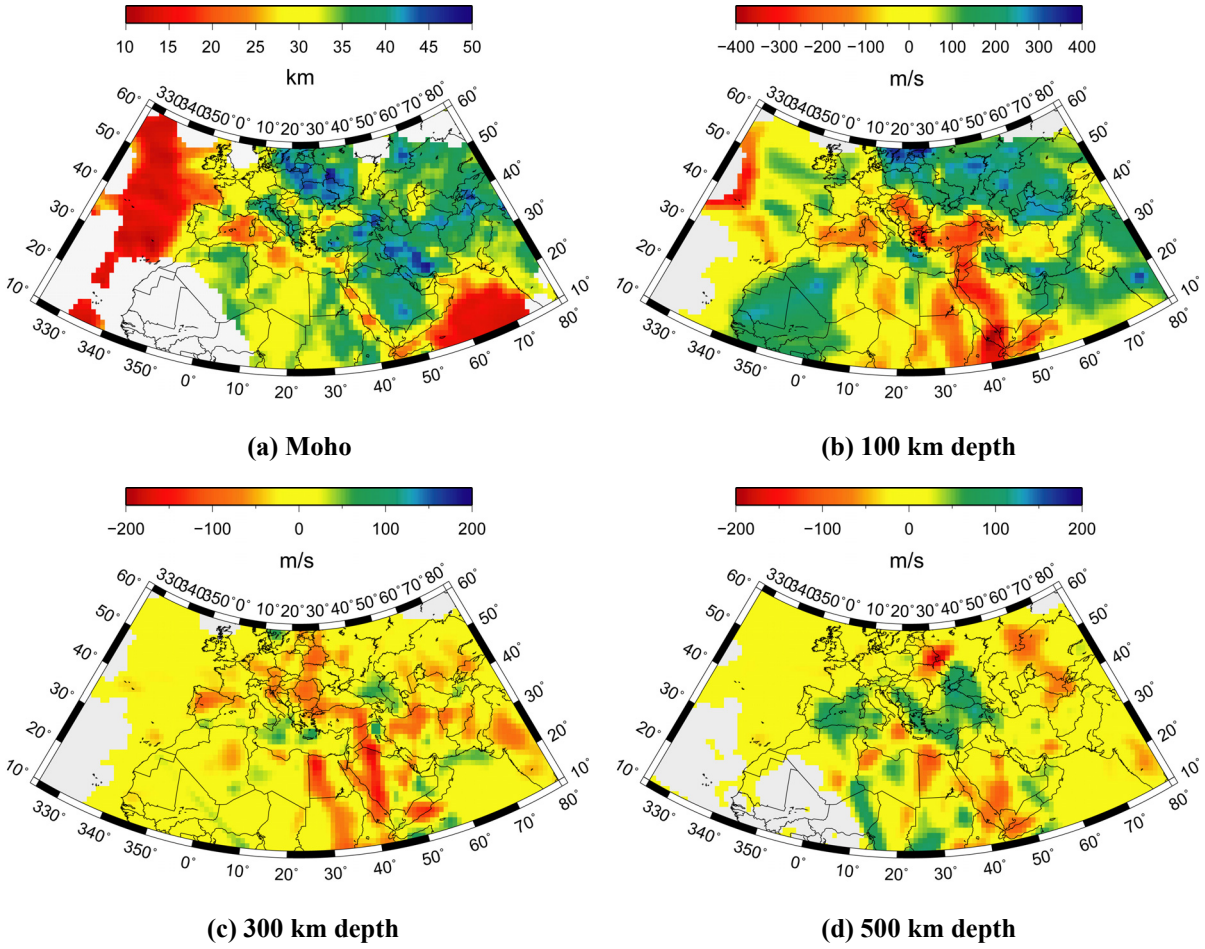

(a) Moho **(b) 100 km depth**

(c) 300 km depth **(d) 500 km depth**

Figure 3. Moho and velocity perturbations resulting from our joint inversion. Moho map (a) and velocity perturbations at 100 km (b), 300 km (c), and 500 km depth (d) are illustrated.

Conversion of *S*-Velocity Model to *P*-Velocity Model

One way to obtain a *P*-velocity model is to perform *P*-wave arrival time inversion using the equation,

$$\mathbf{G}_\alpha \mathbf{m}_\alpha = \mathbf{d}_\alpha , \quad (1)$$

where $\mathbf{G}_\alpha$ is the sensitivity kernel matrix for *P*-wave arrival times, $\mathbf{m}_\alpha$ is the 3-D *P*-velocity model vector, and $\mathbf{d}_\alpha$ is the teleseismic *P*-wave delay vector which is obtained by subtracting predicted arrival times through a reference model from observed arrival times. However, it is difficult to resolve shallow structure with teleseismic *P*-wave arrival time data because of poor resolution for shallow depth. Therefore, we have to find another way to get *P*-velocity model with *P*-wave arrival time data. It would be very promising in the inversion for *P*-velocity model if we can adopt the *S*-velocity model as a preliminary model, because the *S*-velocity model has good resolution for both shallow and deep structure due to our use of regional waveform fits, teleseismic arrival times, Rayleigh-wave group velocities, and Moho depth constraints.

We assume that *P*-wave velocity anomalies in m/s scale are very close to the *S*-wave velocity anomalies in m/s scale in our study area if temperature dominates the for cause of the velocity perturbations based on results in et al. (2004) in which similarity between *P*- and *S*-velocity anomalies is drawn with use of delay time ratio (see Figure 4a). Therefore, it is reasonable to adopt our *S*-velocity model as a starting model in performing a *P*-wave arrival time inversion (Schmid et al., 2008). By multiplication of the *S*-velocity model and *P*-wave sensitivity kernels, we can get predicted *P*-wave delays $\mathbf{d}_{\beta\to\alpha}$ by $\mathbf{m}_\beta$ as in

$$\mathbf{G}_\alpha \mathbf{m}_\beta = \mathbf{d}_{\beta\to\alpha} , \quad (2)$$

where $\mathbf{m}_\beta$ is the 3-D *S*-velocity model in m/s scale, and $\mathbf{d}_{\beta\to\alpha}$ is predicted *P* delays by $\mathbf{m}_\beta$. Then, teleseismic *P*-wave delays $\mathbf{d}_\alpha$ can be divided as

$$\mathbf{d}_\alpha = \mathbf{d}_{\beta\to\alpha} + \mathbf{d}_{res} , \quad (3)$$

where $\mathbf{d}_{res}$ is the residual *P* delay vector which means the difference between $\mathbf{d}_\alpha$ and $\mathbf{d}_{\beta\to\alpha}$. Therefore, Eq. (1) can be rewritten as

$$\mathbf{G}_\alpha (\mathbf{m}_\beta + \mathbf{m}_{new}) = \mathbf{d}_{\beta\to\alpha} + \mathbf{d}_{res} . \quad (4)$$

Eq. (4) is a linear equation, so we extract Eq. (2) from Eq. (4) to perform *P*-wave arrival time inversion for $\mathbf{m}_{new}$ using following equation,

$$\mathbf{G}_\alpha \mathbf{m}_{new} = \mathbf{d}_{res} . \quad (5)$$

A *P*-velocity model is finally obtained by adding $\mathbf{m}_{new}$ to the *S*-velocity model,

$$\mathbf{m}_\alpha = \mathbf{m}_\beta + \mathbf{m}_{new} . \quad (6)$$

The resulting *P*-velocity model with teleseismic *P* arrival time data in Figure 4(b) is shown at various depths in Figure 5. The results are similar to *S*-velocity perturbation results in Figure 3, which means *P*-velocity variations from the *S*-velocity model are small. But higher-velocity anomalies are found in the Alps, Hellenides, Turkey, and the Hindu Kush than in the *S*-velocity model.

Model Evaluation

Distributions of the travel-time residuals with respect to iasp91 and our joint inversion model (Joint Model) are shown in histogram form in Figure 6 for stations AJM, ELL, FRU, MAIO, NIL, PTO, QUE, and SVE. We report both the *L2* norm (mean, standard deviation, STD and variance reduction, VR) and *L1* norm statistics (median, scaled median absolute deviation, SMAD and SMAD reduction, SMADR). The SMAD provides an estimate of the spread of values which is less sensitive to outliers and so is often more appropriate in the presence of non-Gaussian errors. At most stations, SMADR is positive except for ELL, MAIO and QUE.

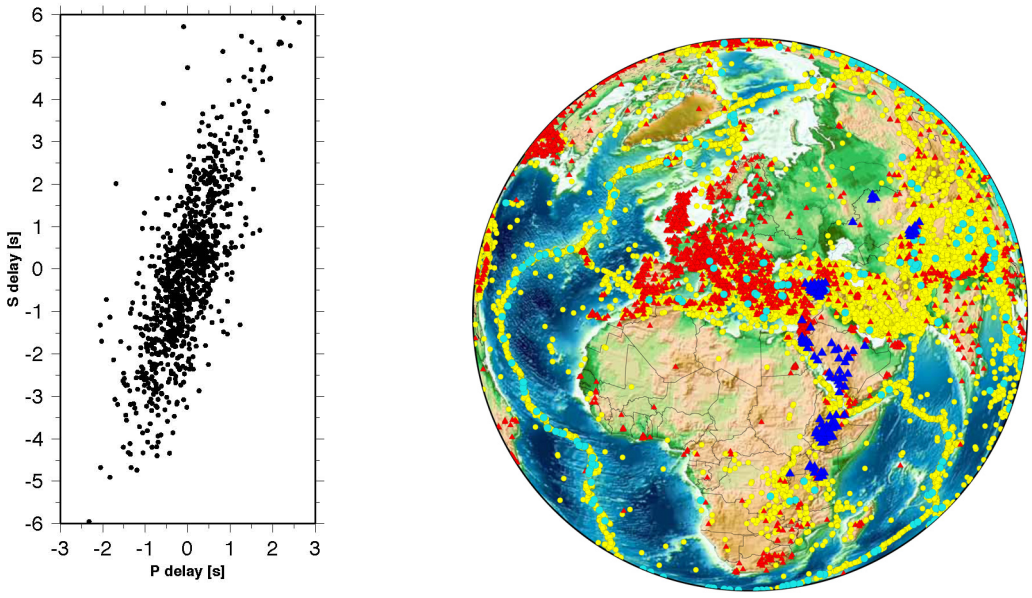

(a) (b)

Figure 4. (a) *S* delays versus *P* delays (Schmid et al., 2004). (b) Events and stations used for teleseismic *P* arrival time estimation. Cyan circles and blue triangles represent events and stations used for relative delay time estimation with MCCC, respectively. Yellow circles and red triangles mean events and stations from the reprocessed ISC catalogue.

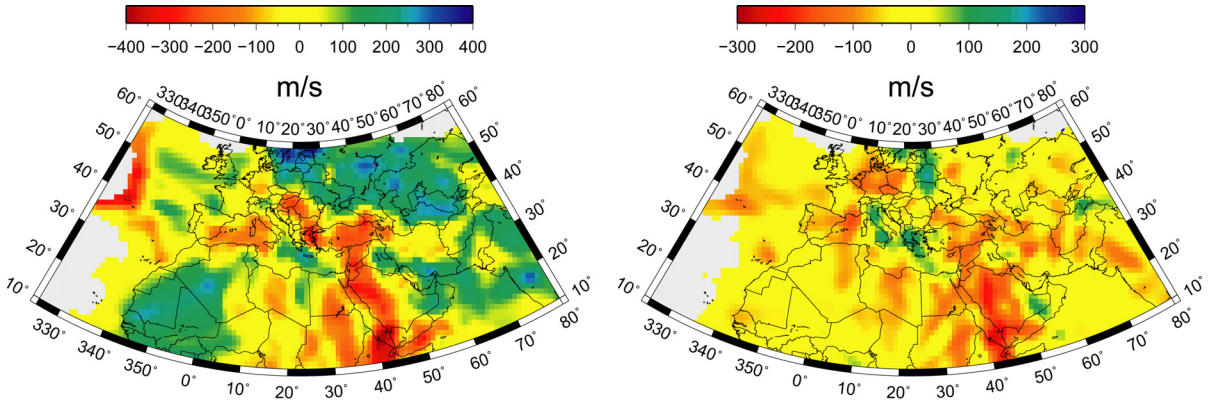

(a) 100 km depth **(b) 200 km depth**

Figure 5. *P*-velocity perturbations at (a) 100 and (b) 200 km depth.

Visually we can evaluate how well the joint inversion model (Joint Model) predicts the data geographically by computing 3D travel-time correction surfaces for some stations. To compute such model-based correction surfaces we subtract the iasp91-predicted time from the Joint Model-predicted time using 3D finite-difference algorithm. Example surfaces are shown in Figure 6 for the stations for a source depth of 10 km; we choose this depth as it represents the average focal depth of the GT25 events (epicenter mislocation of 25 km or less) selected. Color-coded residuals (data-iasp91) from events of focal depth 0 to 20 km are also plotted on top of the surfaces in Figure 6 to provide a visual assessment of the geographic agreement between Joint Model prediction and the data.

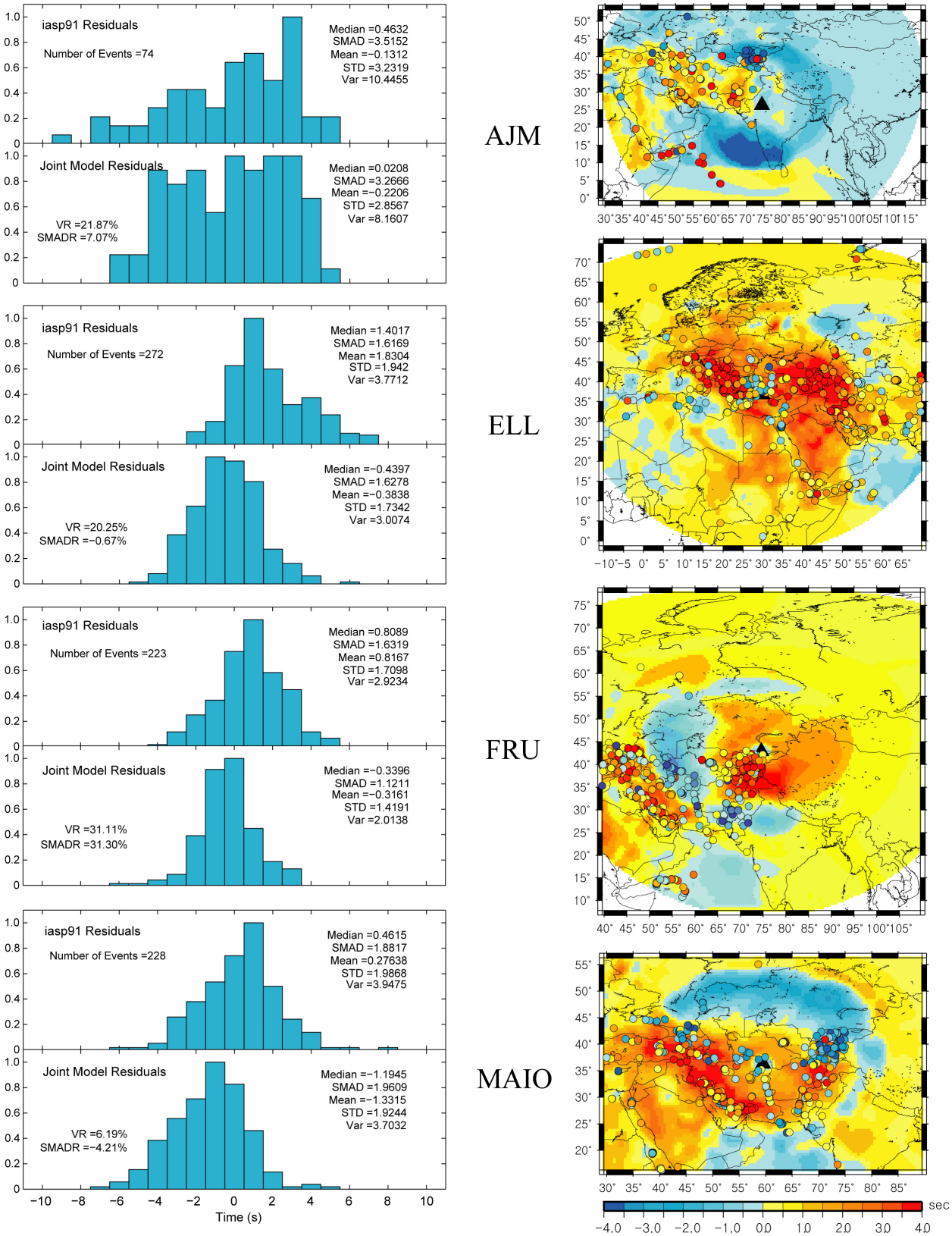
iasp91 Residuals
Number of Events =74
Median =0.4632
SMAD =3.5152
Mean =−0.1312
STD =3.2319
Var =10.4455
Joint Model Residuals
VR =21.87%
SMADR =7.07%
Median =0.0208
SMAD =3.2666
Mean =−0.2206
STD =2.8567
Var =8.1607
AJM
iasp91 Residuals
Number of Events =272
Median =1.4017
SMAD =1.6169
Mean =1.8304
STD =1.942
Var =3.7712
Joint Model Residuals
VR =20.25%
SMADR =−0.67%
Median =−0.4397
SMAD =1.6278
Mean =−0.3838
STD =1.7342
Var =3.0074
ELL
iasp91 Residuals
Number of Events =223
Median =0.8089
SMAD =1.6319
Mean =0.8167
STD =1.7098
Var =2.9234
Joint Model Residuals
VR =31.11%
SMADR =31.30%
Median =−0.3396
SMAD =1.1211
Mean =−0.3161
STD =1.4191
Var =2.0138
FRU
iasp91 Residuals
Number of Events =228
Median =0.4615
SMAD =1.8817
Mean =0.27638
STD =1.9868
Var =3.9475
Joint Model Residuals
VR =6.19%
SMADR =−4.21%
Median =−1.1945
SMAD =1.9609
Mean =−1.3315
STD =1.9244
Var =3.7032
MAIO
Time (s)
sec

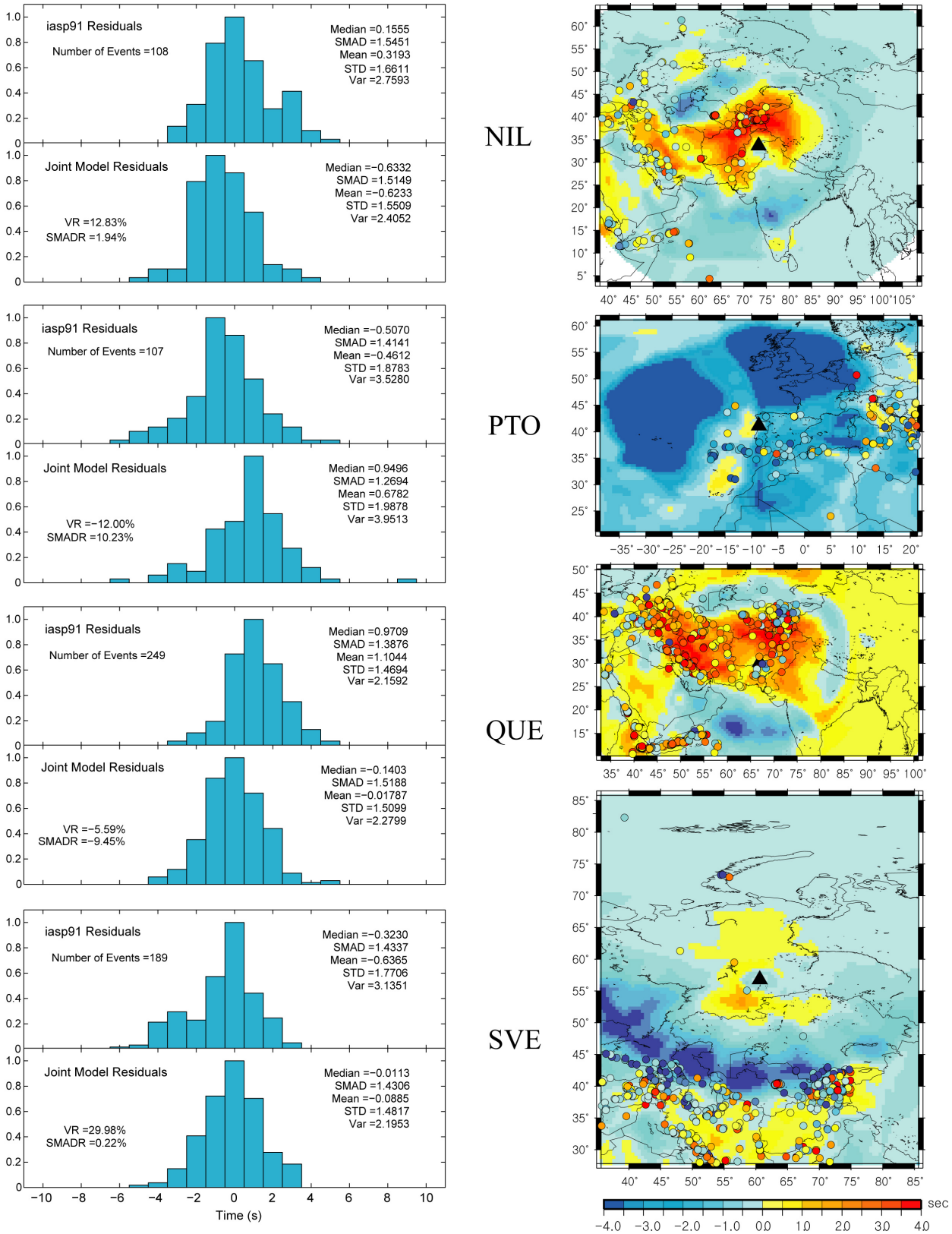

Figure 6. Histograms of travel-time residuals for both models at stations AJM, ELL, FRU, MAIO, NIL, PTO, QUE, and SVE along with the travel-time residual surfaces (Joint Model-iasp91).

CONCLUSIONS AND RECOMMENDATIONS

Through a joint inversion of teleseismic *S*-wave arrival time delays, waveform fits of regional *S*- and Rayleigh waves, group velocity measurements of fundamental-mode Rayleigh waves, and independent constraints on Moho depth, we have achieved considerable variance reduction in each data set simultaneously. The new 3-D *S*-velocity model is converted to a *P*-velocity model with teleseismic *P* arrival times and the *P*-velocity model is used for travel-time prediction. Our model generally produces better prediction than the iasp91 1D model. SMADR is not reduced exceptionally at stations ELL, MAIO and QUE, but mean and median are closer to zero at station ELL and QUE in Joint Model residuals, which means our model succeeded in finding average velocity perturbations. Better refined results could be achieved by substituting our poorly resolved crust with CRUST2.0 and refining the *P*-velocity model.

ACKNOWLEDGEMENTS

We acknowledge information gleaned from Dr. E. R. Engdahl from a personal communication in 2007.

REFERENCES

Benoit, M. H., A. A. Nyblade, T. J. Owens, and G. Stuart (2006), Mantle transition zone structure and upper mantle *S* velocity variations beneath Ethiopia: Evidence for a broad, deep-seated thermal anomaly, *Geochem. Geophys. Geosyst*. 7: Q11013, doi:10.1029/2006GC001398.

DeMets, C. R.G. Gordon, D. F. Argus, and S. Stein (1990). Current plate motions, *Geophys. J. Int*. 101: 425–478.

Engdahl, E.R., van der Hilst, R. and Buland, R. (1998). Global teleseismic earthquake relocation with improved travel times and procedures for depth determination, *Bull. Seis. Soc. Am*. 88: 722–743.

Marone, F. S. Van der Lee, and D. Giardini (2003). Joint inversion of local, regional, and teleseismic data for crustal thickness in the Eurasia-Africa plate boundary region, *Geophys. J. Int*. 154: 499–514.

Marone, F., S. Van der Lee, and D. Giardini (2004). 3-D upper mantle *S*-velocity model for the Eurasia-Africa plate boundary region, *Geophys. J. Int*. 158: 109–130.

Mooney, W.D., G. Laske, and T.G. Masters (1998). CRUST 5.1: A global crustal model at 5° x 5°, *J. Geophys. Res*. 103: 727–747.

Nolet, G. (1990). Partitioned waveform inversion and 2-dimensional structure under the network of autonomously recording seismographs, *J. Geophys. Res*. 95: 8499–8512.

Park, Y., A. A. Nyblade, A. J. Rodgers, and A. Al-Amri (2007). Upper mantle structure beneath the Arabian Peninsula and northern Red Sea from teleseismic body wave tomography: Implication for the origin of Cenozoic uplift and volcanism in the Arabian Shield, *Geochem. Geophys. Geosyst*. 8: Q06021, doi:10.1029/2006GC001566.

Pasyanos, M. E. (2005). A varible-resolution surface wave dispersion study of Eurasia, North Africa, and surrounding regions, *J. Geophys. Res*. 110: B12301, doi:10.1029/2005JB003749.

Röhm, A. H. E., H. Bijwaard, W. Spakman, and J. Trampert (2000), Effects of arrival time errors on traveltime tomography, *Geophys. J. Int*. 142: 270–276.

Schmid, C., S. van der Lee, and D. Giardini (2004), Delay times and shear wave splitting in the Mediterranean region, Geophys. J. Int. 159: 275–290.

Schmid, C., S. van der Lee, J. C. Vandecar, E. R. Engdahl, and D. Giardini (2008). 3-dimensional S-velocity of the mantle in the African-Eurasia plate boundary region from phase arrival times and regional waveforms, *J. Geophys. Res*. 113: B03306, doi:10.1029/2005JB004193.

VanDecar, J.C., and R.S. Crosson (1990), Determination of teleseismic relative phase arrival times using multi-channel cross-correlation and least-squares, *Bull. Seism. Soc. Am*. 80: 150–169.

Van der Lee, S. and G. Nolet (1997). Upper-mantle S-velocity structure of North America, *J. Geophys. Res*. 102: 22,815–22,838.